

# Detailed analysis of the mean diameter and diameter distribution of single wall carbon nanotubes from their optical response

X. Liu,<sup>1</sup> T. Pichler,<sup>1,2</sup> M. Knupfer,<sup>1</sup> M.S. Golden,<sup>3</sup> J. Fink<sup>1</sup>, H. Kataura,<sup>4</sup> and Y. Achiba<sup>4</sup>

<sup>1</sup> *Institute for Solid State and Materials Research Dresden, P.O. Box 270016, D-01171 Dresden, Germany*

<sup>2</sup> *Institut für Materialphysik, Universität Wien, Strudlhofgasse 4, A-1090 Wien, Austria.*

<sup>3</sup> *Van der Waals-Zeeman Institute, University of Amsterdam, Valckenierstraat 65, NL - 1018 XE Amsterdam, The Netherlands.*

<sup>4</sup> *Faculty of Science, Tokyo Metropolitan University, 1-1 Minami-Ohsawa, Hachioji, Tokyo 192-0397, Japan*  
(December 2, 2024)

We report a detailed analysis of the optical properties of single wall carbon nanotubes with different mean diameters as produced by laser ablation. From a combined study of optical absorption, high resolution electron energy-loss spectroscopy in transmission and tight binding calculations we were able to accurately determine the mean diameter and diameter distribution in bulk SWCNT samples. In general, the absorption response can be well described assuming a Gaussian distribution of nanotube diameters and the predicted inverse proportionality between the nanotube diameter and the energy of the absorption features. A detailed simulation enabled not only a determination of the mean diameter of the nanotubes, but also gives insight into the chirality distribution of the nanotubes. The best agreement between the simulation and experiment is observed when only nanotubes within  $15^\circ$  of the armchair axis are considered. The mean diameters and diameter distributions from the optical simulations are in very good agreement with the values derived from other bulk sensitive methods such as electron diffraction, x-ray diffraction and Raman scattering.

## I. INTRODUCTION

Since the discovery of carbon nanotubes<sup>1</sup>, a great deal of attention has been focused on this entirely new class of nanoscale materials. Due to their unusual geometry, their structural and electronic properties, these carbon nanostructures are viewed as promising building blocks for molecular electronics<sup>2</sup>. In particular, single-wall carbon nanotubes (SWCNT) are currently being intensively investigated worldwide since they possess unique and intriguing electronic properties, being either semiconducting or metallic depending on their geometrical structure defined by their chirality<sup>3,4</sup>. After an effective production method of SWCNT was discovered<sup>5</sup>, a huge number of investigations were initiated. However, in all production methods available today (laser desorption<sup>5</sup>, carbon arc method<sup>6</sup>, HPCO (high pressure CO decomposition)<sup>7</sup>, and chemical vapor deposition (CVD)<sup>8</sup>) the produced SWCNT are formed as a polydisperse mixture with various diameters and chiralities. Although claims have been made for the formation of a SWCNT lattice with only one type of (10,10) nanotubes<sup>9</sup>, generally speaking the process of synthesizing nanotubes of only a single diameter and chirality is still beyond our reach.

A first step in a systematic approach towards improved selectivity during the SWCNT production process is a feedback of information coming from a reliable characterization of the mean diameter and diameter distribution in the produced raw SWCNT material. Several different methods have been applied to gain this information. On a local scale the distribution of SWCNT diameters has been analyzed using transmission electron microscopy (TEM)<sup>10</sup>. From TEM studies, for material

synthesized using laser ablation (in general) a Gaussian diameter distribution was observed, whereas from other processes such as CVD and HPCO, the SWCNT diameters are found to be spread over a wider range without a simple distribution function<sup>7</sup>. The big disadvantage of TEM in this context is that it is nanoscale and thus that one can never be sure that one has obtained a result truly representative of the bulk SWCNT diameter distribution. Consequently, a number of bulk sensitive methods which provide information regarding the diameter distribution have been applied. Since the SWCNT produced by laser ablation, carbon arc and HPCO are predominantly organized in bundles, X-ray<sup>10,11</sup> and electron diffraction are suited to characterize the SWCNT mean diameter and diameter distribution from the diffraction pattern of the bundle lattice. Such diffraction-based methods possess the disadvantage that they are insensitive to any individual (and hence non-bundled) SWCNT present in the sample. This is a grave set-back in the analysis of material from the CVD route, as this material generally contains a significant proportion of individual nanotubes.

The second, bulk sensitive characterization method utilizes the optical properties of the SWCNT. From consideration of the folding of the Brillouin zone of a graphene sheet resulting from the new boundary conditions generated by the conceptual 'rolling up' to form a nanotube, tight binding (TB) calculations have led to a simple relationship between the SWCNT diameter and the energy of the optical interband transitions of the SWCNT<sup>12</sup>. From the same type of calculations one third of the possible SWCNTs - those with wrapping vectors  $(n, m)$  where  $n - m = 3l$  ( $l = 0, 1, 2, \dots$ ) - are predicted to be metallic. All other tubes are semiconductors. The

unit cell of the SWCNTs strongly depends on the choice of  $n$  and  $m$ . The smallest unit cell is found if  $n = m$  or either  $n$  or  $m$  are zero, and in this case is as large as that of the graphene sheet. Such special nanotubes are called *armchair* (chiral angle  $30^\circ$ ) and *zigzag* (chiral angle  $0^\circ$ ), respectively. All other tubes are called *chiral*. The diameter  $d$  of the tubes is related to the components of the Hamada vector by  $d = a_0\sqrt{m^2 + n^2 + mn}/\pi$  where  $a_0 = 2.46 \text{ \AA}$  is the lattice constant of the graphene plane. Due to the one-dimensional nature of the SWCNTs, their electronic structure exhibits clear van Hove singularities. The energetic separation of the pairs of van Hove singularities is inversely proportional to the tube diameter. The optical response of the SWCNT is dominated by transitions between peaks in the density of states (DOS) of the valence and conduction bands, with momentum conservation only allowing transitions pairs of singularities which are symmetrically placed with respect to the Fermi level. Thus, following the van Hove singularities, the optical transitions in SWCNT are also inversely proportional to the nanotube diameter. For the first two allowed optical transitions in semiconducting SWCNT, it follows that  $E_{11}^S = 2a_0\gamma_0/d$  and  $E_{22}^S = 4a_0\gamma_0/d$ , where  $\gamma_0$  is the tight binding nearest neighbor overlap integral. For the metallic SWCNT, at a first glance the energies of the optical transitions would appear to be proportional to  $E_{11}^M = 6a_0\gamma_0/d$ . However, more recently, it has been pointed out that the density of states of the metallic SWCNT is chirality dependent due to the trigonal warp effect, i.e., the energy contours near the Fermi surface deviate from a circle<sup>13-16</sup>. This leads to a splitting of the singularities in metallic tubes, which is maximal for the zigzag variety.

Experimentally, it has been demonstrated that electron energy-loss spectroscopy (EELS) in transmission and optical absorption spectroscopy are powerful tools in the study of the mean electronic properties of bulk samples of SWCNT<sup>17-19</sup>. From both the EELS analysis and the optical absorption data, several distinct spectral features are observed for energies below 3 eV. These features have been related to the above mentioned interband transitions between the van Hove singularities in the electronic DOS of the semiconducting and metallic SWCNT. The inverse proportionality on the nanotube diameter allows a first determination of the mean diameter and diameter distribution under the assumption of a scaling factor<sup>11,18</sup>. In addition, the higher energy resolution available in optical absorption allows the identification of fine structure within the individual absorption features<sup>18</sup>. Since this fine structure is related to individual SWCNT, or groups of SWCNT with similar diameter, the analysis of such data would appear to offer information as to whether the formation process of SWCNT leads to the existence of preferred wrapping angles in the nanotube vector map<sup>3,18</sup>.

Complementary to optical spectroscopy, the same inverse proportionality between energy and nanotube diameter is found in Raman spectroscopy for the so-called

radial breathing mode (RBM) of nanotubes which is observed as an intense features at around  $200 \text{ cm}^{-1}$ . The energy of the RBM scales as  $C/d$  where  $d$  is the diameter of the tubes and  $C = 234 \text{ cm}^{-1}\text{nm}$  is a constant determined recently from an *ab initio* calculation<sup>26</sup>. The Raman response for this mode is subject to a strong dependence upon the energy of the exciting laser used in the Raman experiment. Whereby photo-selective resonance scattering<sup>17,27-29,32</sup> has been demonstrated to be responsible for both the fine structure in the RBM lineshape and an oscillatory behavior of the spectral moments<sup>11</sup>. Consequently, analysis of Raman data recorded using different laser lines has also been frequently applied as a tool to analyze the SWCNT mean diameter and diameter distribution in both bulk and nanoscopic samples<sup>28,32</sup>. However, one has to be aware that a simple line shape analysis of the Raman response is misleading and the resonance Raman scattering and the oscillations of the spectral moments have to be included in the detailed analysis<sup>11</sup>. One remaining uncertainty in the Raman analysis of SWCNT bundles regards the size of the intertube interaction within a bundle. The exact strength of this interaction is still unknown, although it is known to lead to a stiffening of the RBM. From a model calculation using a non-orthogonal tight-binding approximation, a intertube interaction induced upshift of the RBM of about 8-12 % was calculated<sup>30</sup>. This upshift of the RBM has also used to estimate the size of the nanotube bundles<sup>29</sup>.

As the physical properties of SWCNT depend so crucially upon their diameter, it is an important challenge to arrive at a sound understanding of how their diameter can be measured in bulk samples. This serves not only our fundamental understanding of SWCNT as a materials class, but also is a valuable component in our thinking about SWCNT as a realistic technological material. In this paper, we present a detailed analysis of the optical properties of laser ablation-produced SWCNT, with mean nanotube diameters ranging from 0.9 nm to 1.5 nm. We use data from high resolution EELS in transmission together with optical absorption spectroscopy and electron diffraction, to examine the relationship between the observed optical transitions and the mean nanotube diameter. As a first step, the mean diameter of the SWCNT was obtained from electron diffraction data taken in the EELS spectrometer from large SWCNT bundles assuming a hexagonal SWCNT lattice. In the next step, a detailed analysis of the the optical absorption spectra of SWCNT with different mean diameters is performed within the framework of a tight binding model. The results show that a best agreement between the simulated and measured optical absorption is reached when the simulation only includes SWCNT chiralities up to maximally  $15^\circ$  away from the armchair axis. Finally, the resulting mean diameter and diameter distribution from the detailed optical analysis of the nanotubes is compared to the results from the other bulk sensitive methods of nanotube diameter determination, namely,

electron diffraction, X-ray diffraction, and Raman scattering.

## II. EXPERIMENTAL

SWCNT with different mean diameters and diameter distributions were produced by laser ablation as described previously<sup>17,18</sup>. Thin films of SWCNT with an effective thickness about 1000 Å were prepared by dropping an acetone suspension of SWCNT onto KBr single crystals. After the KBr was dissolved in distilled water, the films were transferred to a standard 200 mesh platinum electron microscopy grid and heated for 6 hours in ultra high vacuum up to 600°C, which has been shown to remove the organic contamination in the SWCNT films<sup>10</sup>. The EELS measurements were carried out using a purpose-built 170 keV spectrometer<sup>21</sup>. The energy and momentum resolution were chosen to be 180 meV and 0.03 Å<sup>-1</sup> for the low energy loss function and electron diffraction, respectively. The optical absorption data were measured on the same samples as used for EELS using a Bruker 88 covering from the near-infrared region to the ultraviolet with a spectral resolution of 2 cm<sup>-1</sup> (0.25 meV). All experiments were performed at room temperature and the EELS measurements are carried out under ultra-high vacuum conditions.

## III. RESULTS AND DISCUSSION

### A. Mean diameter from electron diffraction

During the formation process in the laser ablation oven van der Waals forces lead to the formation of bundles of SWCNT in which the individual nanotubes are arranged within a hexagonal lattice. These bundles usually consist of SWCNT with a finite diameter distribution<sup>22</sup>, are believed to be representative of the mean diameter of bulk samples. Consequently, as mentioned above, the diffraction pattern of the bundle lattice can be used to obtain a first estimation of the SWCNT mean diameter, as the intertube distance is mainly dependent on the nanotube diameter.

We are able to carry out electron diffraction in the EELS spectrometer by setting the energy-loss to zero. Figure 1 shows the raw electron diffraction data from SWCNT samples with six different nanotube mean diameters. We label these samples A to F, and they contain SWCNT with diameters covering a total range of 0.2 Å<sup>-1</sup> to 6.0 Å<sup>-1</sup>. The strong increase in intensity in the raw diffraction data at low  $q$  seen in Fig. 1 is small angle scattering originating from large objects in the sample, e.g., catalyst particles, amorphous carbon, etc. Generally, the peaks in a SWCNT diffraction profile can be divided into two parts. The low- $q$  part of the diffraction pattern (below 2 Å<sup>-1</sup>) is only sensitive to the crystalline order in the

bundle, thus corresponding to SWCNT bundle diffraction. The high- $q$  range (above 2 Å<sup>-1</sup>) is sensitive to the internal structure of individual tubes, whereby the broad peaks near 2.9 Å<sup>-1</sup> and 5 Å<sup>-1</sup> originate from the (1 0 0) and (1 1 0) graphite in-plane reflections, respectively<sup>23</sup>. The interplane reflection (0 0 2), i.e., the peak near 2 Å<sup>-1</sup> is very weak. The absence of a peak corresponding to the (0 0 4) reflection proves the absence of multiwall carbon nanotubes in the samples<sup>24</sup>. In the context of these experiments, all peaks coming from the bundle diffraction can be used to estimate the mean diameter of the nanotubes. The first-order diffraction peak (1 0) near 0.4-0.5 Å<sup>-1</sup> from the hexagonal bundle lattice has the highest intensity. As can be seen from the dashed arrow in the inset to Fig. 1, there is a strong upshift in the (1 0) feature on going from sample A to F, indicating a decrease of the mean nanotube diameter. In general, the intensity of the first diffraction peak corresponds is sensitive to the crystallinity and size of bundles. Normally, the bigger size of bundle, the higher crystalline in SWCNT sample. Therefore, higher intensity in the first electron diffraction peak can provide a way to roughly estimate the relative bundle size in different SWCNT soot samples. So, from inspection of Fig. 1, one can conclude that the SWCNTs in samples A, B, C and D (i.e those with larger mean diameter) have more crystalline or simply larger bundles compared to the samples containing thinner SWCNTs.

In order to obtain the mean diameter from electron diffraction, the position of this (1 0) peak is used. Assuming a perfect hexagonal lattice, the intertube distance is equal to the tube diameter plus the two times the van der Waals radius (ca. 0.335 nm). The resultant values for the mean nanotube diameter for the six samples A, B, C, D, E, and F are 1.46 nm, 1.37 nm, 1.34 nm, 1.30 nm, 1.08 nm, and 0.91 nm, respectively.

Furthermore, once the mean diameter has been arrived at, the expected positions of the high-order diffraction peaks can also be calculated using the hexagonal lattice model and compared to the experimental data. If the first bundle peak is weak, its position can also be extrapolated from the positions of the higher-order peaks. In Fig. 2 the position of the first three diffraction peaks – i.e., (1 0), (1 1), and (1 2) – are plotted versus the mean diameter (derived from the position of the [1 0] peak) for the six different nanotube samples. In each case the solid lines depict the calculated peak position for the ideal hexagonal structure. As the first peak was used as the calibrated standard, it naturally lies on the theoretical line. For the high-order peaks, there are only small deviations from the predicted behaviour, showing that the hexagonal lattice is a good description of the nanotubes within the crystalline bundles.

## B. Low energy interband transitions

As mentioned above, the energetic position of the interband transitions between the DOS singularities are inversely dependent on the diameter of SWCNT<sup>12</sup>. EELS in transmission measured using low momentum transfers probes the optical limit, thus the low-energy peaks in the loss function are due to collective excitations caused by these optically allowed transitions<sup>19</sup>. Later, analogous results for the low energy interband transitions were obtained from optical absorption spectroscopy<sup>17,18</sup>. It is interesting to compare the results from these the two different experiments for the same samples. Typical EELS and optical results for SWCNT with 1.3 nm mean diameter (sample D) are depicted in Fig. 3. The left panel shows the loss function at a momentum transfer  $q = 0.1 \text{ \AA}^{-1}$  between 0 and 9 eV which covers the excitations related solely to the SWCNT  $\pi$  electron system. The strong peak at ca. 6 eV is the so-called  $\pi$  plasmon, which is the collective excitation of the SWCNT  $\pi$  electrons. The first three loss peaks below 3.0 eV (i.e.,  $L_{11}^S$ ,  $L_{22}^S$ , and  $L_{11}^M$ ) are ascribed to interband transition from EELS measurement. In the right panel a typical optical absorption spectrum of the same nanotubes is depicted. The inset shows the absorbance after subtracting the contributions from the high energy interband transitions. From Fig. 3 it is obvious that the contributions of the low energy interband transitions are very similar in the two experiments and can be easily compared. The peaks related to transitions between the first and second pairs of DOS singularities in semiconducting nanotubes (designated  $E_{11}^S$  and  $E_{22}^S$ ) are observed at about 0.9 and 1.5 eV, whereas the position of the feature due to the transitions between the first pair of DOS singularities in metallic nanotubes (designated  $E_{11}^M$ ) is about 2 eV. Here it should be mentioned that since in EELS we are probing collective excitations (proportional to  $\text{Im}(-1/\epsilon)$ ), the peak positions are slightly upshifted as compared to optical absorption which is proportional to the imaginary part of  $\epsilon$ , i.e., the peak position of  $L_{11}^S$  is always higher than that of  $E_{11}^S$ . In principle, one could use a Kramers-Kronig-analysis to derive the absorption data from the loss function data (see Ref. 19).

In Fig. 4 we show the experimental results for the interband transitions  $E_{11}^S$ ,  $E_{22}^S$ , and  $E_{11}^M$  from the SWCNT samples with six different mean diameters (samples A to F from Fig. 1). The left panel shows the EELS data and the right panel optical absorption results (from which the high energy background has been subtracted). The dashed lines in Fig. 4 indicate the mean positions (center of gravity) of the SWCNT interband transitions for the peaks from the semiconducting SWCNT as well as the metallic SWCNT. It is obvious that the energy of these transitions depends strongly on the SWCNT diameter. With increasing SWCNT diameter, all the interband transitions peaks shift to lower energy. Whereas in optical absorption a distinct fine structure is observed, especially for the very thin SWCNT, in the EELS mea-

surements no fine structure could be observed, simply due to the lower energy resolution in EELS. Due to the above mentioned slight upshift of the peak positions in EELS as compared to in optical absorption, the peak positions in the following analyses are always referred to those in the optical data unless otherwise stated. For the samples E and F (which have the smallest SWCNT mean diameters), the fine structure in optical absorption is strongly pronounced for the  $E_{22}^S$  and  $E_{11}^M$  peaks. This is a natural consequence of the greater energetic separation of the DOS singularities in these nanotubes, meaning that each sub-spectrum from a particular SWCNT diameter is more easily distinguished from the signal from neighboring diameters. As a consequence of the pronounced fine structure in these peaks in the optical absorption spectra, the mean energetic positions for the  $E_{22}^S$ , and  $E_{11}^M$  features can be only extracted with some uncertainty.

It is now interesting to compare the center of gravities of the three low energy absorption peaks  $E_{11}^S$ ,  $E_{22}^S$  and  $E_{11}^M$  with the above mentioned predictions within the tight binding, or TB-model. The results are shown in Fig. 5 for the six samples as a function of the inverse SWCNT diameter, which was estimated from the electron diffraction data discussed earlier. The solid lines are the predictions from the TB-model using an overlap integral  $\gamma_0 = 3.0$  eV which is well established value<sup>11,12</sup>. It is obvious that the  $E_{22}^S$  and  $E_{11}^M$  peaks show in general a good agreement with the model, and only display small deviations at smaller SWCNT diameters, which can be explained by a small decrease of the overlap integral  $\gamma_0$ <sup>11</sup>. However, for all SWCNT material studied, the first optical transition is always upshifted compared to the theoretical prediction. Recently, the Coulomb interaction has been taken into account in the calculation of the theoretical spectra of SWCNT using a conventionally screened Hartree-Fock approach with an effective-mass approximation scheme<sup>20</sup> and this approach has been used to explain the experimental data<sup>25</sup>. With the inclusion of the Coulomb interaction between electrons, the optical transition energies between the valence bands and the corresponding conduction bands shift to the higher energies. This blue shift is a net result of two opposing effects. On the one hand electron correlation enlarges the band gap and on the other hand excitonic effects would be expected to lead to a red shift of the first absorption feature. The second optical transition energy, however, scarcely shifts on switching on the correlation as the two competing effects described above appear to cancel each other almost exactly.

Therefore, bearing these facts in mind, the energetic position of the second absorption peak provides a better measure of the SWCNT diameter when analyzing the data within the framework of the TB-model (in which correlation effects are not fully accounted for). Interestingly, the impact of the Coulomb interaction on the  $E_{11}^S$  peak is also strongly dependent upon the SWCNT diameter. Considering the fact that the  $E_{22}^S$  peak (which shows little net result of correlation effects) should occur

at an energy twice that of the  $E_{11}^S$  peak, the impact of the Coulomb interaction effects can then be easily visualized by looking at the diameter dependence of the average value of the energy positions of the centers of gravity of  $E_{11}^S$  and  $E_{22}^S$ . In Fig. 6, a summary of these effects for all the measured nanotube samples is plotted as a function of SWCNT mean diameter. It can be clearly seen that for the fatter SWCNT the effects are smaller than for the very thin SWCNT. This diameter dependence cannot solely be explained by a slightly reduced TB overlap integral for very thin SWCNT ( $d < 1.1$  nm), and confirms that additional effects going beyond the one electron TB model have to be taken into account. Nevertheless, having said that, a detailed analysis of the  $E_{22}^S$  and  $E_{11}^M$  peaks still allows a very accurate determination of the SWCNT mean diameter and diameter distribution, and can even provide indications of whether there is a chirality dependence in the SWCNT production process.

### C. Detailed analysis of the optical absorption

As mentioned above, the energetic position of the absorption peaks of SWCNT are proportional to the overlap integral and inversely proportional to the diameter of the SWCNT<sup>12</sup>. Since the bulk samples consist of a distribution of SWCNT with mean different diameters and chirality, a pronounced fine structure corresponding to groups of SWCNT is observed in the optical absorption spectra. The profile of the  $E_{22}^S$  and  $E_{11}^M$  features in the SWCNT spectra provides suitable data from which to determine the mean diameter and the diameter distribution of the investigated SWCNT from a direct simulation of the absorption spectra after subtracting the background. Under the assumptions described below, this approach contains only the SWCNT mean diameter and diameter distribution as freely adjustable parameters. The assumptions underlying the analysis routine are:

- a) If present in the sample, all the SWCNT in the vector map give the same contribution to the overall optical absorption. This is tantamount to saying that the transition matrix element is independent of the SWCNT chirality or diameter.
- b) The absorption intensity is dominated by transitions between pairs of corresponding van Hove singularities in the SWCNT DOS (e.g.  $E_{11}$  and not  $E_{12}$ ), and the broadening due, for example, to life-time effects is also independent of chirality and diameter.
- c) The SWCNT in the sample have a Gaussian distribution of diameters.
- d)  $\gamma_0$  is independent of the chirality or diameter.

Given these points, the corresponding absorption intensity from SWCNTs with Hamada vector  $(n, m)$  and diameter  $d(n, m)$  is modulated by a Gaussian function. The absorption profile of the bulk SWCNT sample can be written as

$$I(E) = f * \sum_{n,m} \exp\left[-\frac{(d_{n,m} - d_0)^2}{2(\Delta d)^2}\right] \frac{w}{(E - E_{ii})^2 + (w/2)^2} \quad (1)$$

where  $f$  is an overall scaling factor and  $w$  (ca. 40 meV) describes broadening of each single transition due to the finite lifetime of the band-to band transition and the finite resolution of the spectrometer. The energy positions  $E_{ii}$  ( $i=1, 2, 3$ ) are taken from the separation between the maxima of the van Hove singularities in the SWCNT electronic DOS. Recently, it has been pointed out that the detailed form of the van Hove singularities in the one-dimensional electronic density of states of SWCNT are chirality-dependent. The deviations from a circle in the energy contours near the Fermi points produce a splitting of the DOS singularities in metallic nanotubes (the so-called trigonal warp effect)<sup>13</sup>. The magnitude of this effect depends on the chiral angle of the carbon nanotube and is maximal for metallic zigzag nanotubes and zero for armchair nanotubes<sup>13-16</sup>. An approximate analytical expression for the density-of-states singularities in single-walled carbon nanotubes has been derived<sup>16</sup>, including the energy splitting for an arbitrary chiral angle in metallic nanotubes. From the work of Ref. 16 semi-conducting nanotubes are shown to fall into two classes and transitions between their van Hove singularities will have a corresponding energy shift. Since in our analysis we pick up the value from the maxima of van Hove singularities in the calculated DOS, this effect is implicitly included. In this way, the experimental results can be fitted by varying the mean diameter  $d_0$  and the diameter distribution  $\Delta d$  in equation [1].

Fig. 7 illustrates the results of such an individual fit to the first three absorption peaks of SWCNT sample B. In this case, the fitting has been performed including all the  $(n, m)$  pairs in the SWCNT vector map and took a  $\gamma_0$  value of 3.0 eV. The solid line indicates the as-measured data after background subtraction, and the dotted line is the result of the fit. For the  $E_{11}^S$  peak, the above mentioned blue-shift has been taken into account (in the form of a somewhat larger  $\gamma_0$  value). For this sample we arrive at a mean diameter  $d$  of 1.37 nm and diameter distribution  $\Delta d$  of 0.09 nm, in good agreement with the electron diffraction results.

Although the gross features of the experimental data are well reproduced by the fit, there are still small deviations regarding the fine structure. One possibility in this regard would be that not all nanotubes are created with equal probability in the production process - there could be SWCNT produced with a preferred chirality. From a simple treatment of previous optical results from SWCNT produced by laser ablation<sup>18</sup>, it has indeed been suggested that nanotubes formed lie closer to the armchair axis than to the zigzag direction in the SWCNT vector map. Thus it is natural in our fitting of the optical data to re-investigate this hypothesis by repeating the analysis of this high-resolution optical data taking as

a basis a preferred selection of nanotube chiralities. To do this, we divided the vector map into slices of  $5^\circ$  chiral angle and repeated the fit for each slice. In general, a good agreement is observed for chiral angles close to the armchair axis.

As can be seen from Fig. 8, by far the worst agreement with the experimental data is reached by only considering SWCNT near to the zigzag axis (chiral angles between  $0-15^\circ$ ). The result is much better when all the possible nanotubes are included in the fit ( $0-30^\circ$ ). Interestingly, a closer inspection of the results for the peak derived from transitions between the second pair of van Hove singularities (Fig. 8b), shows that the quality of the fit is still further improved when only nanotubes with chiral angles between  $15-30^\circ$  are taken in to account. We note here that this trend as regards the fit results is fully consistent for all of the optical data considered here, independent of the mean SWCNT diameter. Consequently, we can conclude that within the framework of the analysis described here, we have gained additional evidence that SWCNT are preferentially formed closer to the armchair rather than zigzag axis during the synthetic process. However, in consideration of the simplifying assumptions made in the analytical approach taken here we cannot obtain information about the exact distribution of nanotubes across the chiralities from bulk measurement. Further analysis methods focused on the individual SWCNT such as STS-STM<sup>31,34</sup>, resonant Raman<sup>32</sup>, small area TEM diffraction<sup>22,33</sup> are required. In the context of these data and the fit results it is interesting to compare the apparent preferential formation of SWCNT with chiral angles between  $15-30^\circ$  with conclusions reached from other chirality sensitive measurements of the individual SWCNT<sup>33,34</sup> which all have confirmed that chiralities of SWCNT produced by laser ablation are close to armchair.

Finally, completing this study of the information regarding SWCNT diameter and diameter and chirality distribution that can be extracted from bulk optical absorption data, we cross-check the mean nanotube diameter obtained from the simulation of the optical absorbance with the results from the other bulk, diameter-sensitive methods mentioned earlier. The results of the comparison of x-ray diffraction, resonance Raman scattering, the fitting of the optical data, and electron diffraction are depicted in Fig. 9. The x-axis gives the mean diameter as given by the average over all the bulk SWCNT diameter determination methods. Fig. 9 shows a high degree of consistency between the methods, with the scattering of the mean diameter values from the average being less than 0.05 nm. The same holds for the diameter distribution, as shown in the inset of Fig. 9.

## IV. CONCLUSIONS

A detailed analysis of the optical properties of SWCNT with different mean diameters as produced by laser ablation was presented. From a combined study of optical absorption spectroscopy, high resolution electron energy-loss spectroscopy in transmission and tight binding calculations, we were able to accurately determine the mean diameter and diameter distribution of the bulk nanotube samples studied. In general, the absorption response could be accurately determined by assuming a Gaussian distribution of SWCNT diameters and applying the inverse proportionality between the SWCNT diameter and the energy of the absorption features predicted by the tight binding model. Small deviations from the TB model are observed for the lowest energy main feature -  $E_{11}^S$  peaks - which are attributed to Coulomb interaction effects. A detailed fit of the optical absorption spectra allows a determination not only the mean diameter and diameter distribution but also enables additional insight to be gained into the possible existence of any chirality dependence during the SWCNT formation process. The best agreement between the simulated spectra and experiment is observed upon restricting the chiral angle of the nanotubes to lie within  $15^\circ$  of the armchair axis. The mean diameter and diameter distribution resulting from the simulation are in very good agreement with the values derived from other bulk sensitive methods such as electron diffraction, X-ray diffraction, and Raman scattering.

### Acknowledgments:

We thank the DFG (FI 439/8-1) and the EU (IST-NID-Project SATURN) for funding. One of us (T.P.) acknowledges financial support from the ÖAW in form of an APART fellowship and thanks the FWF P14146 for funding. H.K. acknowledges a Grant-in-Aid for Scientific Research (A), 13304026 from the Ministry of Education, Science, Sports and Culture of Japan.

- 
- <sup>1</sup> S. Iijima, *Nature (London)* **354**, 56 (1991).
  - <sup>2</sup> C. Dekker, *Phys. Today* **52**, 22 (1999).
  - <sup>3</sup> N. Hamada, S. Sawada and A. Oshiyama, *Phys. Rev. Lett.* **68**, 1579 (1992).
  - <sup>4</sup> R. Saito, M. Fujita, G. Dresselhaus, and M.S. Dresselhaus, *Appl. Phys. Lett.* **60**, 2204 (1992).
  - <sup>5</sup> T. Guo, P. Nikolaev, A. Thess, D.T. Colbert, and R.E. Smalley, *Chem. Phys. Lett.* **243**, 49 (1995).
  - <sup>6</sup> C. Journet, W.K. Maser, P. Bernier, and A. Loiseau, *Nature* **388**, 756 (1997).
  - <sup>7</sup> P. Nikolaev, M.J. Bronikowski, R.K. Bradley, F. Rohmund, D.T. Colbert, K.A. Smith and R.E. Smalley, *Chem. Phys. Lett.* **313**, 91 (1999).

- <sup>8</sup> A. Cassell, J. Raymakers, J. Kong, and H. Dai, *J. Phys. Chem.* **103**, 6484 (1999).
- <sup>9</sup> R.R. Schlittler, J.W. Seo, J.K. Gimzewski, C. Durkan, M.S.M. Saifullah, and M.E. Welland, *Science* **292**, 1136 (2001).
- <sup>10</sup> A.G. Rinzler, J. Liu, H. Dai, C.B. Huffman, F. Rodriguez-Macias, P.J. Boul, A.H. Lu, D. Heymann, D.T. Colbert, R.S. Lee, J.E. Fischer, A. M. Rao, P.C. Eklund, and R. E. Smalley, *Appl. Phys. A: Mater. Sci. Process.* **67**, 29 (1998).
- <sup>11</sup> H. Kuzmany, W. Plank, M. Hulman, Ch. Kramberger, A. Gruneis, Th. Pichler, H. Peterlik, H. Kataura, and Y. Achiba, *Eur. Phys. J. B* **22**, 307 (2001).
- <sup>12</sup> R. Saito, G. Dresselhaus, and M.S. Dresselhaus, *Physical Properties of Carbon Nanotubes* (Imperial College Press, London 1998).
- <sup>13</sup> J.W. Mintmire and C.T. White, *Phys. Rev. Lett.* **81**, 2506 (1998).
- <sup>14</sup> P. Kim, T.W. Odom, J.-L. Huang, and C. M. Lieber, *Phys. Rev. Lett.* **82**, 1225 (1999).
- <sup>15</sup> R. Saito, G. Dresselhaus, and M.S. Dresselhaus, *Phys. Rev. B* **61**, 2981 (2000).
- <sup>16</sup> S. Reich and C. Thomsen, *Phys. Rev. B* **62**, 4273 (2000).
- <sup>17</sup> H. Kataura, Y. Kumazawa, Y. Maniwa, I. Umez, S. Suzuki, Y. Ohtsuka, and Y. Achiba, *Synth. Met.* **103**, 2555 (1999).
- <sup>18</sup> O. Jost, A.A. Gorbunov, W. Pompe, T. Pichler, R. Friedlein, M. Knupfer, M. Reibold, H.-D. Bauer, L. Dunsch, M.S. Golden, and J. Fink, *Appl. Phys. Lett.* **75**, 2217 (1999).
- <sup>19</sup> T. Pichler, M. Knupfer, M.S. Golden, J. Fink, A.G. Rinzler, and R.E. Smalley, *Phys. Rev. Lett.* **80**, 4729 (1998).
- <sup>20</sup> T. Ando, *J. Phys. Soc. Jpn.* **66**, 1066 (1997).
- <sup>21</sup> J. Fink, *Adv. Electron. Electron Phys.* **75**, 121 (1989).
- <sup>22</sup> D. Bernaerts, A. Zettl, N. G. Chopra, A. Thess and R. E. Smalley, *Solid State Commun.* **105**, 145 (1998).
- <sup>23</sup> Y. Maniwa, R. Fujiwara, H. Kira, H. Tou, E. Nishibori, M. Takata, M. Sakata, A. Fujiwara, X. Zhao, S. Iijima, and Y. Ando, *Phys. Rev. B* **64**, 073105 (2001).
- <sup>24</sup> S. Rols, R. Almairac, L. Henrard, E. Anglaret, and J. -L. Sauvajol, *Eur. Phys. J. B* **10**, 263 (1999).
- <sup>25</sup> M. Ichida, S. Mizuno, Y. Tani, Y. Saito, and A. Nakamura, *J. Phys. Soc. Jpn.* **68**, 3133 (1999).
- <sup>26</sup> J. Kürti, G. Kresse, and H. Kuzmany, *Phys. Rev. B* **58**, R8869 (1998).
- <sup>27</sup> A.M. Rao, E. Richter, S. Bandow, B. Chase, P.C. Eklund, K.A. Williams, S. Fang, K.R. Subbaswamy, M. Menon, A. Thess, R.E. Smalley, G. Dresselhaus, and M.S. Dresselhaus, *Science* **275**, 187 (1997).
- <sup>28</sup> S. Bandow, S. Asaka, Y. Saito, A. M. Rao, L. Grigorian, E. Richter, and P.C. Eklund, *Phys. Rev. Lett.* **80**, 3779 (1998).
- <sup>29</sup> H. Kuzmany, B. Burger, M. Hulman, J. Kürti, A.G. Rinzler, and R.E. Smalley, *Europhys. Lett.* **44**, 518 (1998).
- <sup>30</sup> L. Henrard, E. Hernandez, and P. Bernier, *Phys. Rev. B* **60**, R8521 (1999); L. Henrard, V. N. Popov, and A. Rubio, *Phys. Rev. B* **64**, 205403 (2001).
- <sup>31</sup> J.W.G. Wildoer, L.C. Venema, A.G. Rinzler, R.E. Smalley, and C. Dekker, *Nature* **391**, 59, (1998).
- <sup>32</sup> A. Jorio, R. Saito, J. H. Hafner, C. M. Lieber, M. Hunter, T. McClure, G. Dresselhaus, and M. S. Dresselhaus, *Phys. Rev. Lett.* **86**, 1118 (2001).
- <sup>33</sup> J. M. Cowley, P. Nikolaev, A. Thess, and R. E. Smalley *Chem. Phys. Lett.*, **265**, 379 (1997); L. Henrard, P. Bernier, C. Journet, and A. Loiseau, *Synth. Met.* **103**, 2533 (1999).
- <sup>34</sup> L.C. Venema, J.W. G. Wildoer, J.W. Janssen, S.J. Tans, H. L. J. Temminck Tuinstra, L. P. Kouwenhoven, and C. Dekker *Science* **283**, 52 (1999).

FIG. 1. Electron diffraction profiles of SWCNT with different mean diameters from six different samples: A (the fattest nanotubes) to F (the thinnest nanotubes). The inset shows the spectra enlarged in the region of the bundle peak.

FIG. 2. Position of the first three electron diffraction features originating from the hexagonal SWCNT bundle lattice as a function of SWCNT mean diameter (full circles). The solid lines are the calculated behaviour for an ideal hexagonal SWCNT lattice structure as described in the text.

FIG. 3. (a) Loss function of SWCNT with 1.3 nm mean diameter (sample D) recorded at  $q=0.1 \text{ \AA}^{-1}$  between 0 and 9 eV.  $L_{11}^S$ ,  $L_{22}^S$ , and  $L_{11}^M$  are interband transition in loss function from EELS measurement. (b) Optical absorption spectra of the same SWCNT between 0 and 3 eV. The inset shows the absorbance in the range of  $E_{11}^S$ ,  $E_{22}^S$ , and  $E_{11}^M$  interband transitions after subtraction of the contributions from the high energy interband transitions.

FIG. 4. (a) Loss function in the region of the low energy interband transitions for SWCNT with different mean diameters recorded with  $q=0.1 \text{ \AA}^{-1}$ . (b) Optical absorption spectra (after background subtraction) from SWCNT with mean diameters as indicated.

FIG. 5. Observed energy of the three lowest energy interband transitions estimated from the center of gravity of each peak in the optical absorption spectrum (full circles) as a function of the inverse mean diameter (from electron diffraction) of the SWCNT. The solid line shows the results derived from the commonly-used tight-binding-based formula with  $\gamma_0 = 3.0 \text{ eV}$  and  $a_0 = 0.142 \text{ nm}$ .

FIG. 6. The difference between the energy of the lowest lying interband transition ( $E_{11}^S$ ) and half of that of the second transition ( $E_{22}^S$ ) in SWCNT with different mean diameters as a function of the SWCNT mean diameter. Deviation from the value 0.5 is an indication of Coulomb interaction effects, which most strongly affect the energy position of  $E_{11}^S$  (for details see text).

FIG. 7. Simulation of the first three optical absorption peaks of sample B with  $d=1.37$  nm upon the basis of tight binding calculations. Nanotubes of all chiralities are included. The solid line is the measured spectrum (with background subtracted); the dashed line represents the results of the simulation.

FIG. 8. The tight-binding-based fitting of the (a)  $E_{22}^S$  and (b)  $E_{11}^M$  optical absorption features of sample A with  $d=1.46$  nm. The solid line is the measured data (background subtracted), and the dashed lines are the simulations using a SWCNT chiral angle distribution as indicated.  $30^\circ$  stands for armchair,  $0^\circ$  for a zigzag nanotube.

FIG. 9. Correlation plot of the SWCNT mean diameters  $d_{method}$  determined by different bulk sensitive methods. The horizontal axis is the SWCNT  $d_{mean}$  averaged over all methods. The Raman and x-ray results are from Ref. 11. The inset shows the plot of the diameter distribution  $\Delta d$  versus different mean diameters.

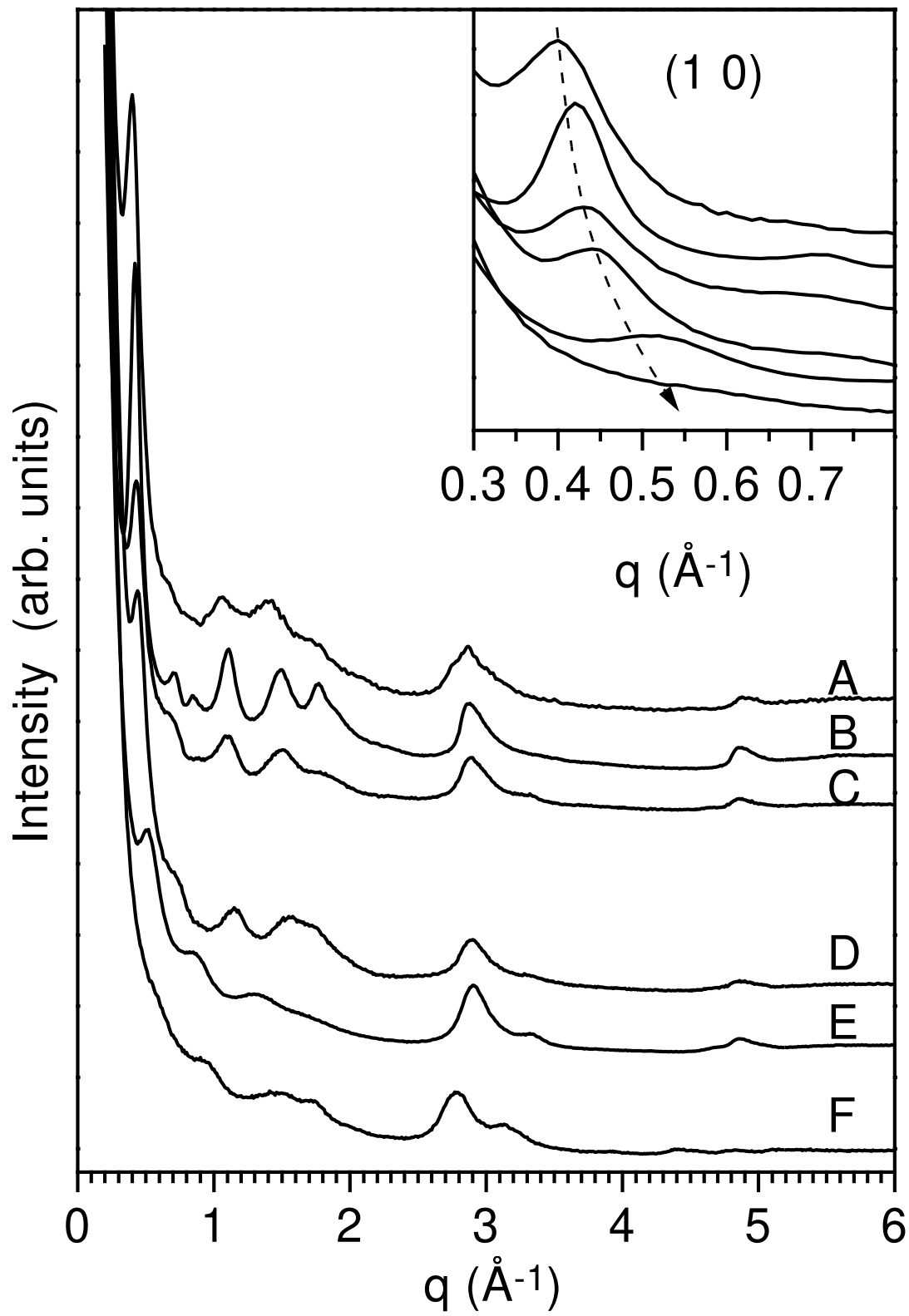


Fig. 1 Liu *et al.*



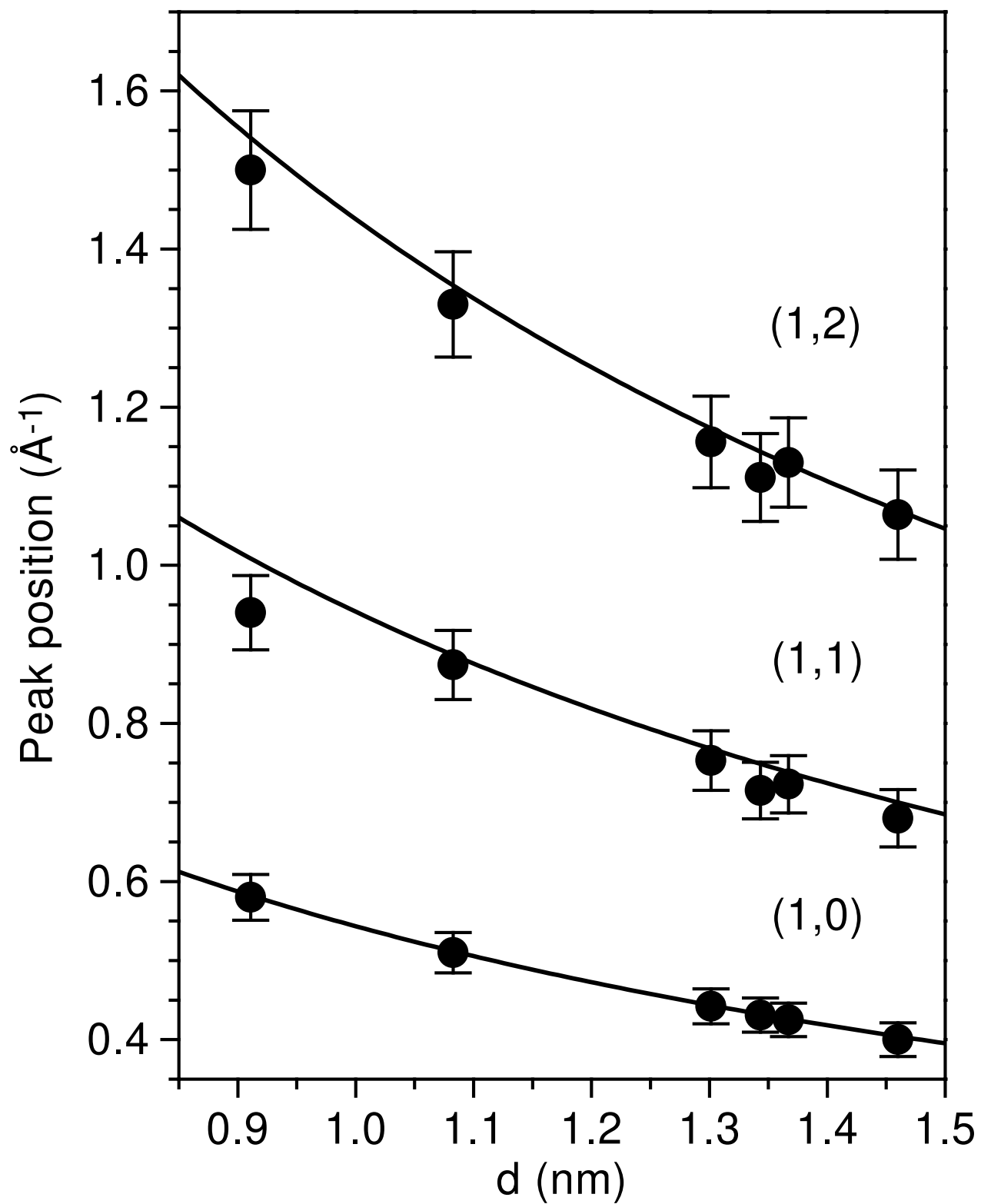
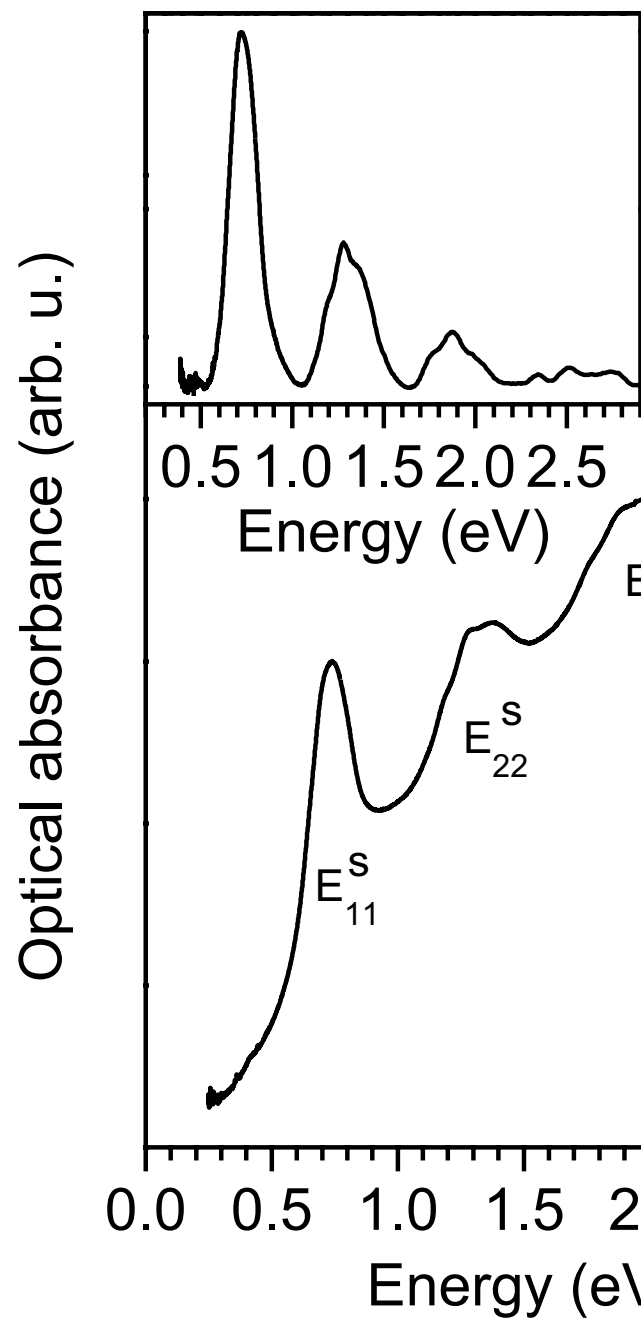
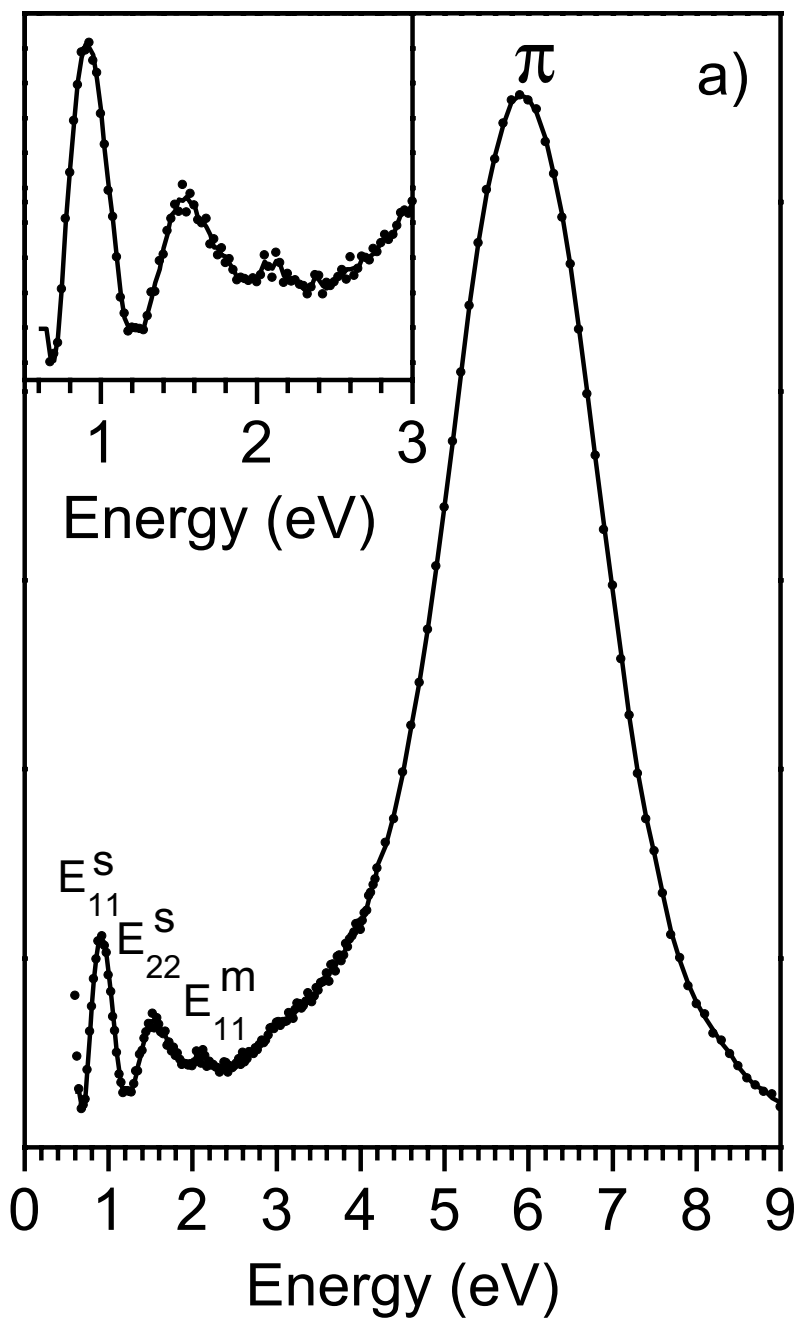
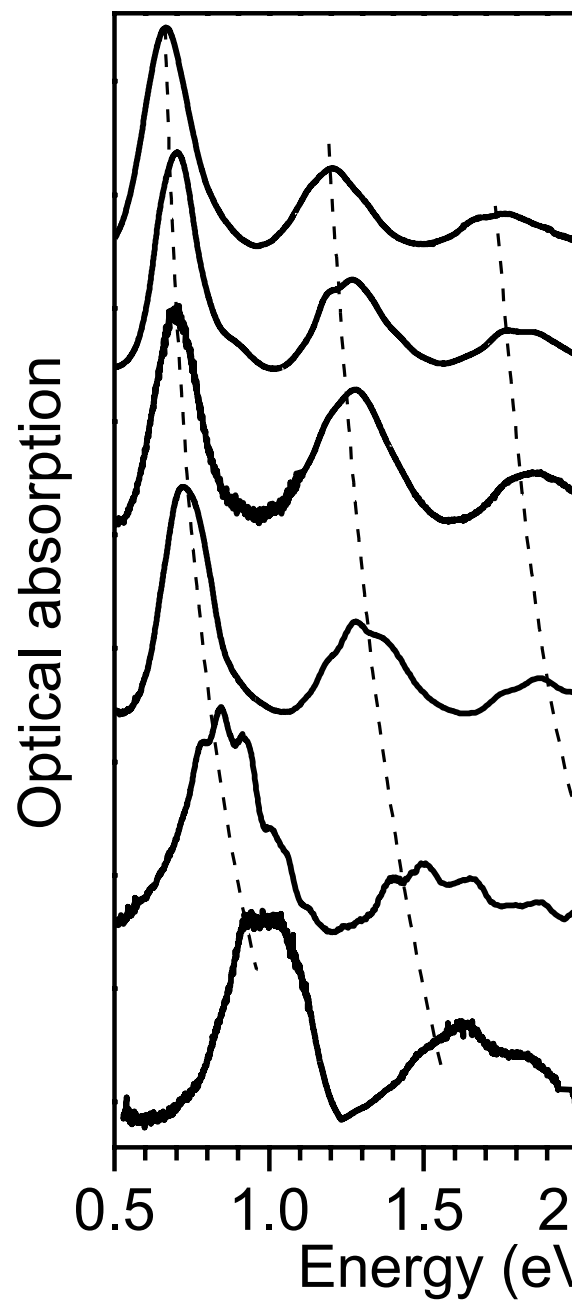
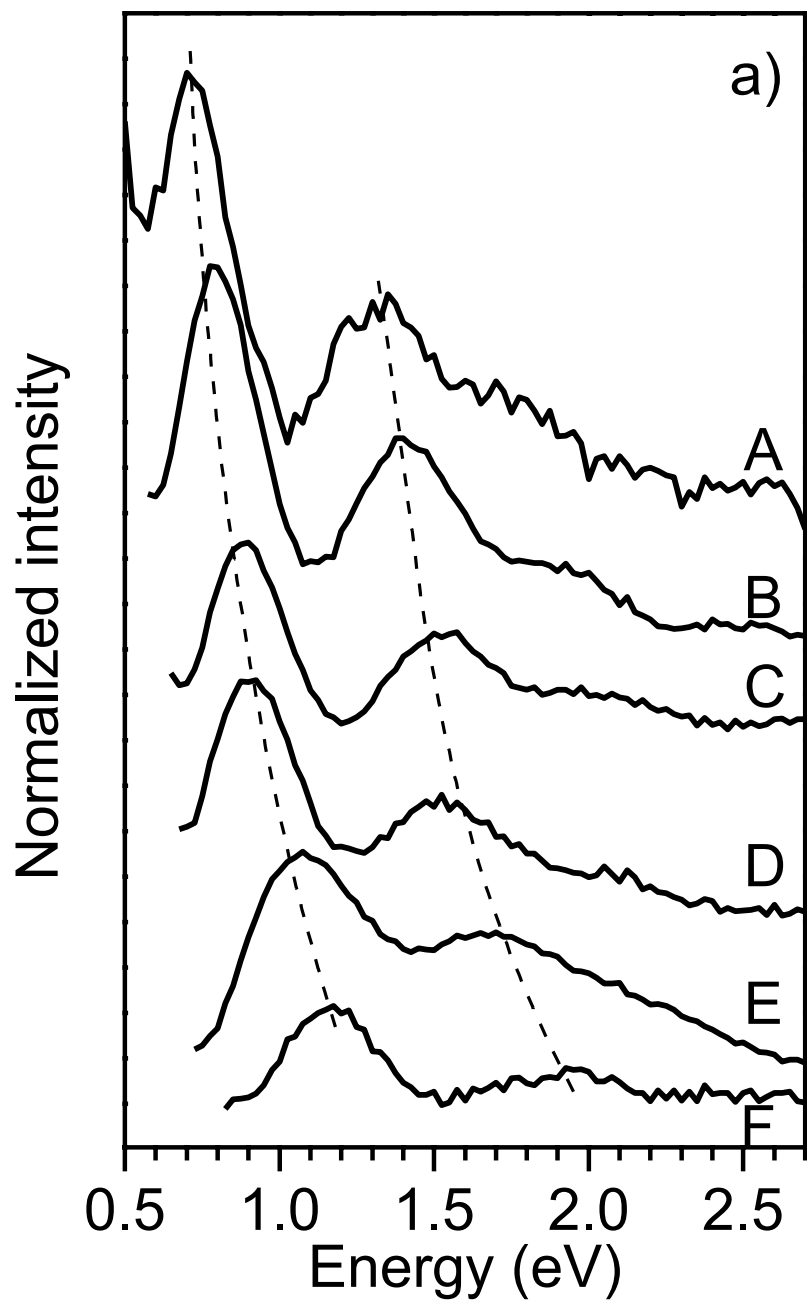


Fig. 2 Liu *et al.*







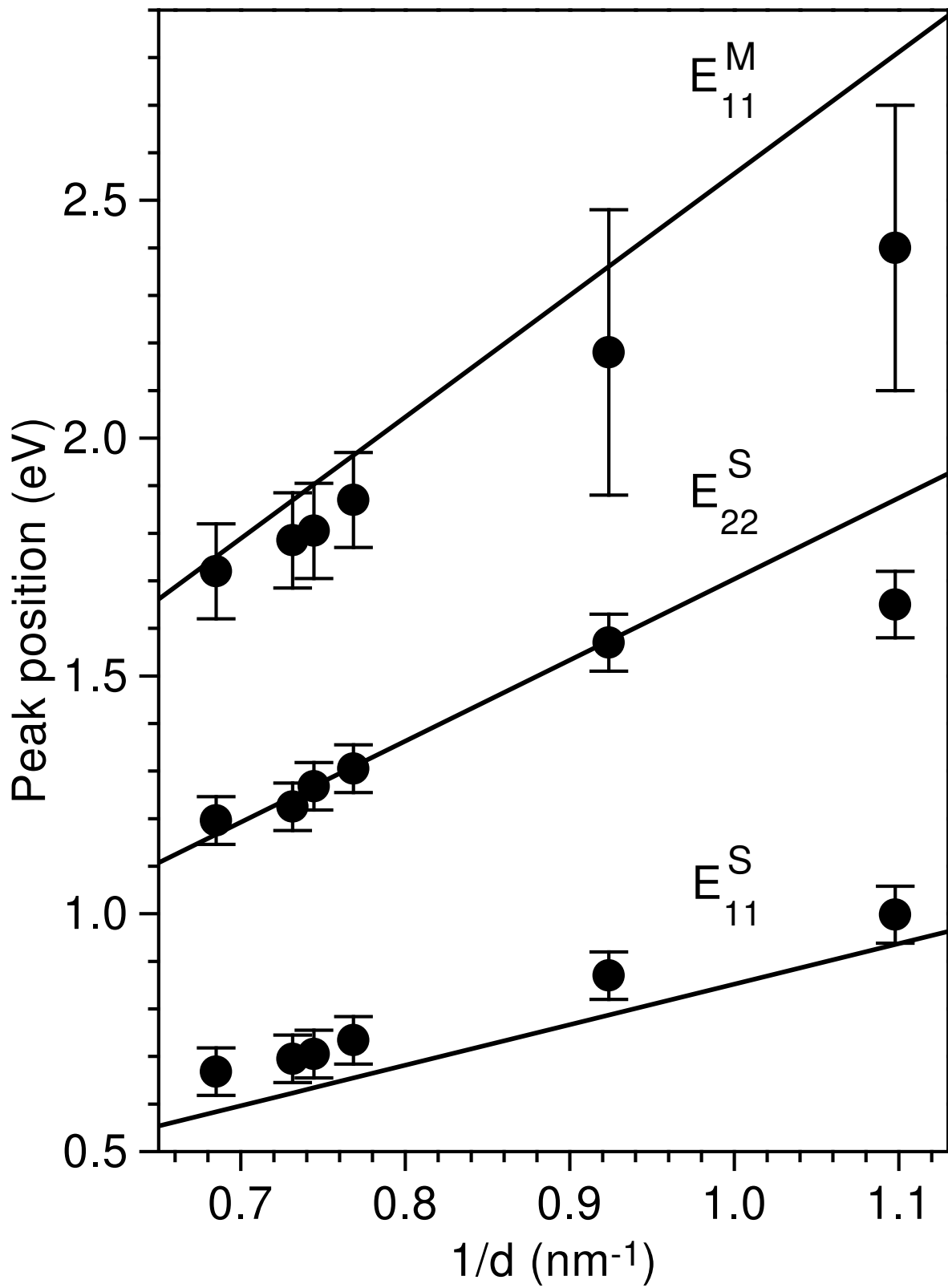


Fig. 5 Liu *et al.*



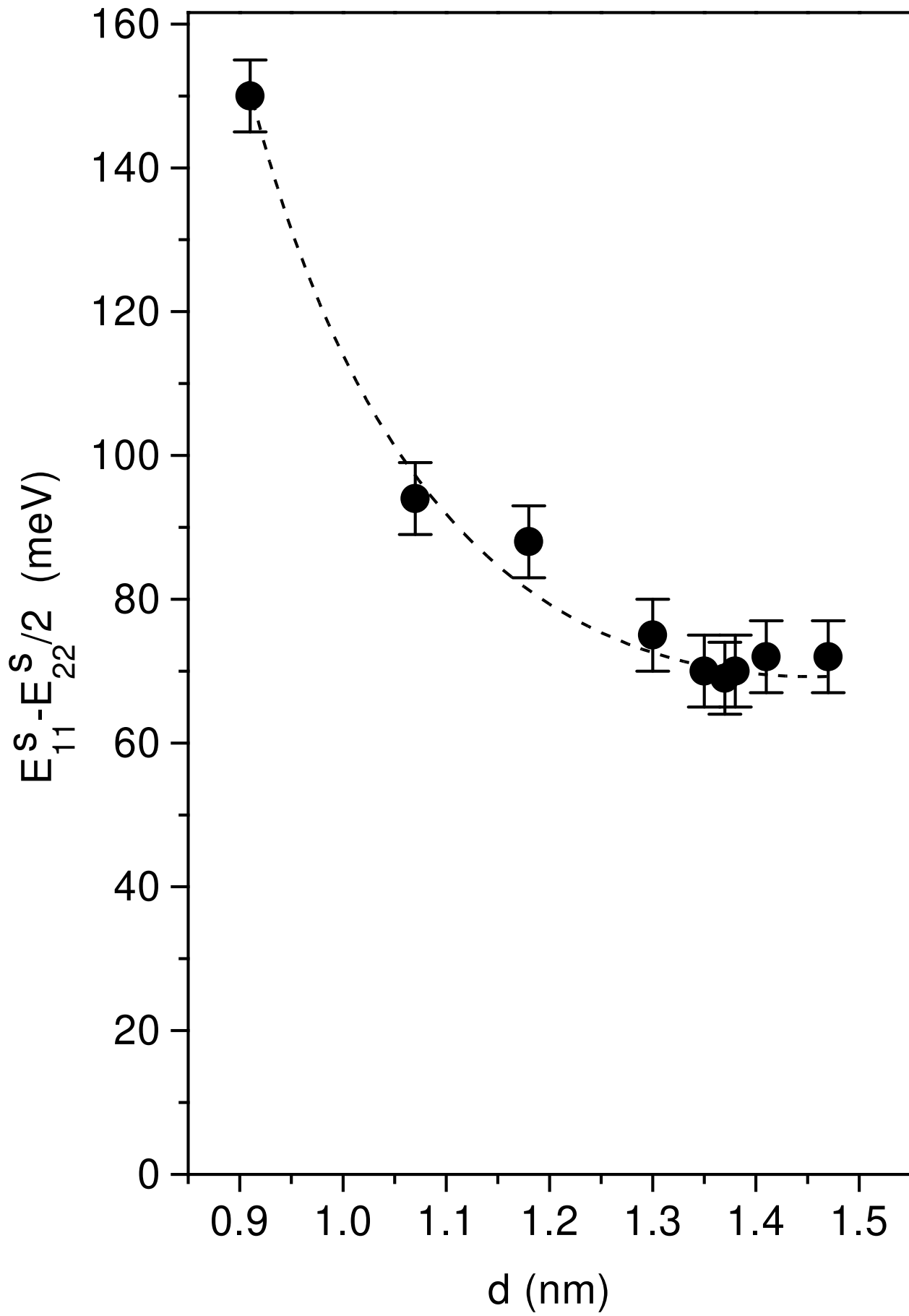


Fig. 6 Liu *et al.*



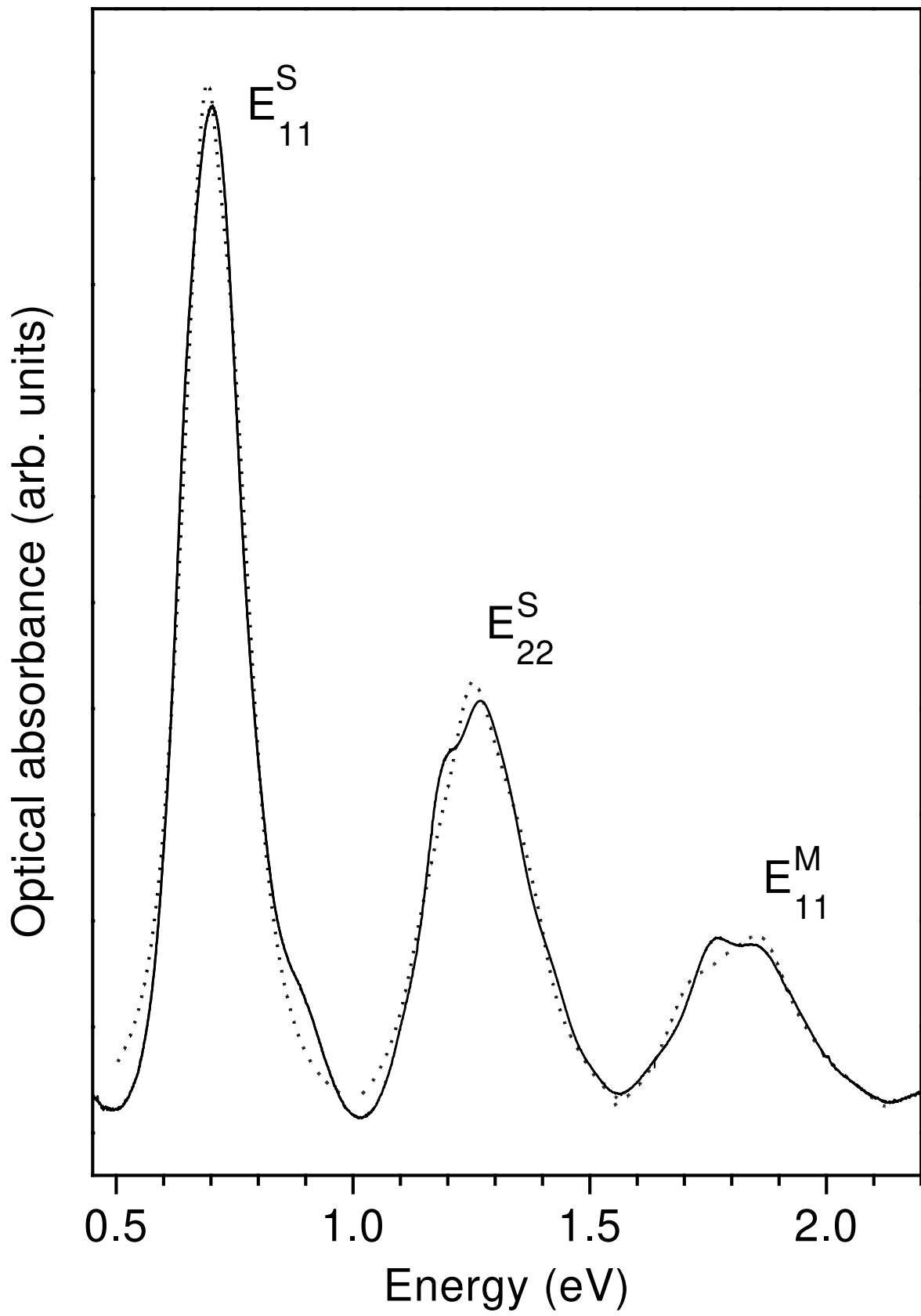
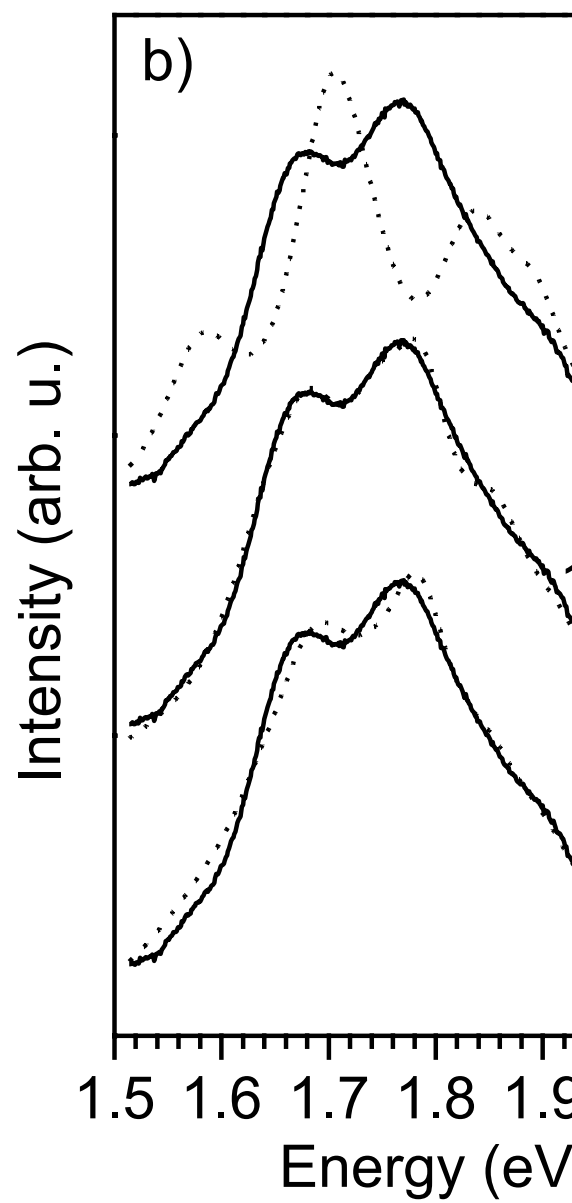
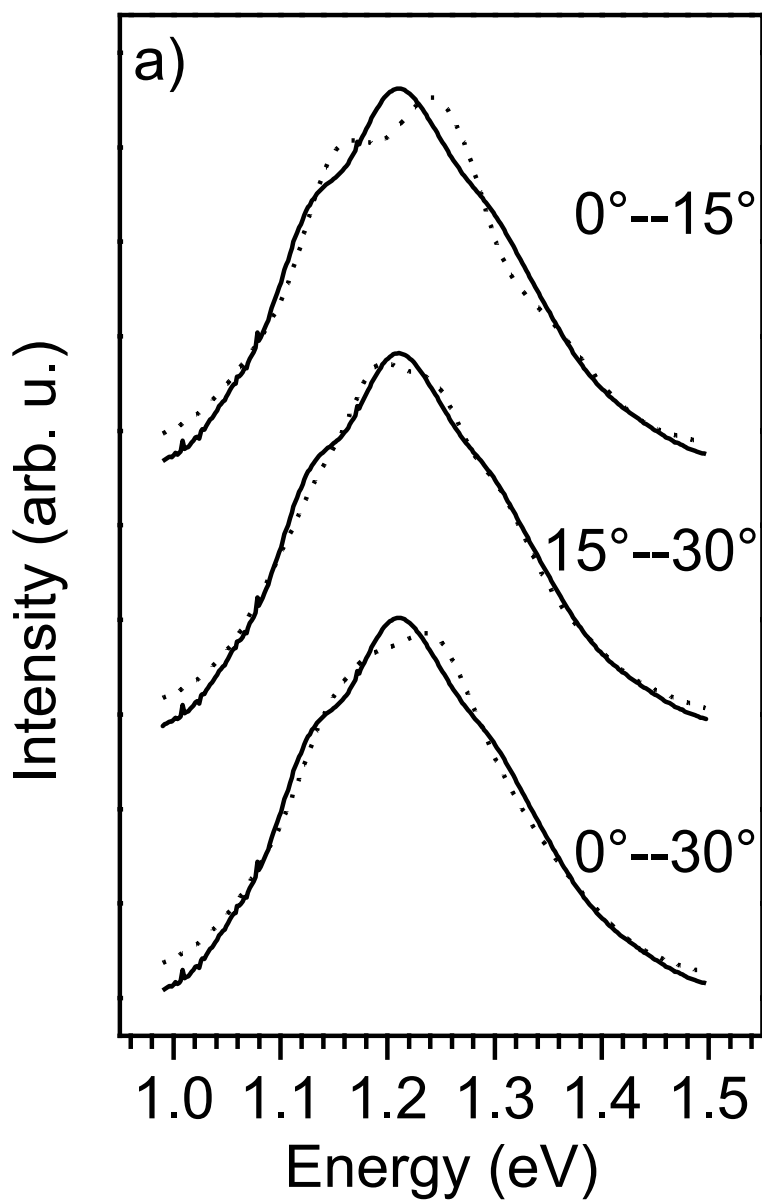


Fig. 7 Liu *et al.*





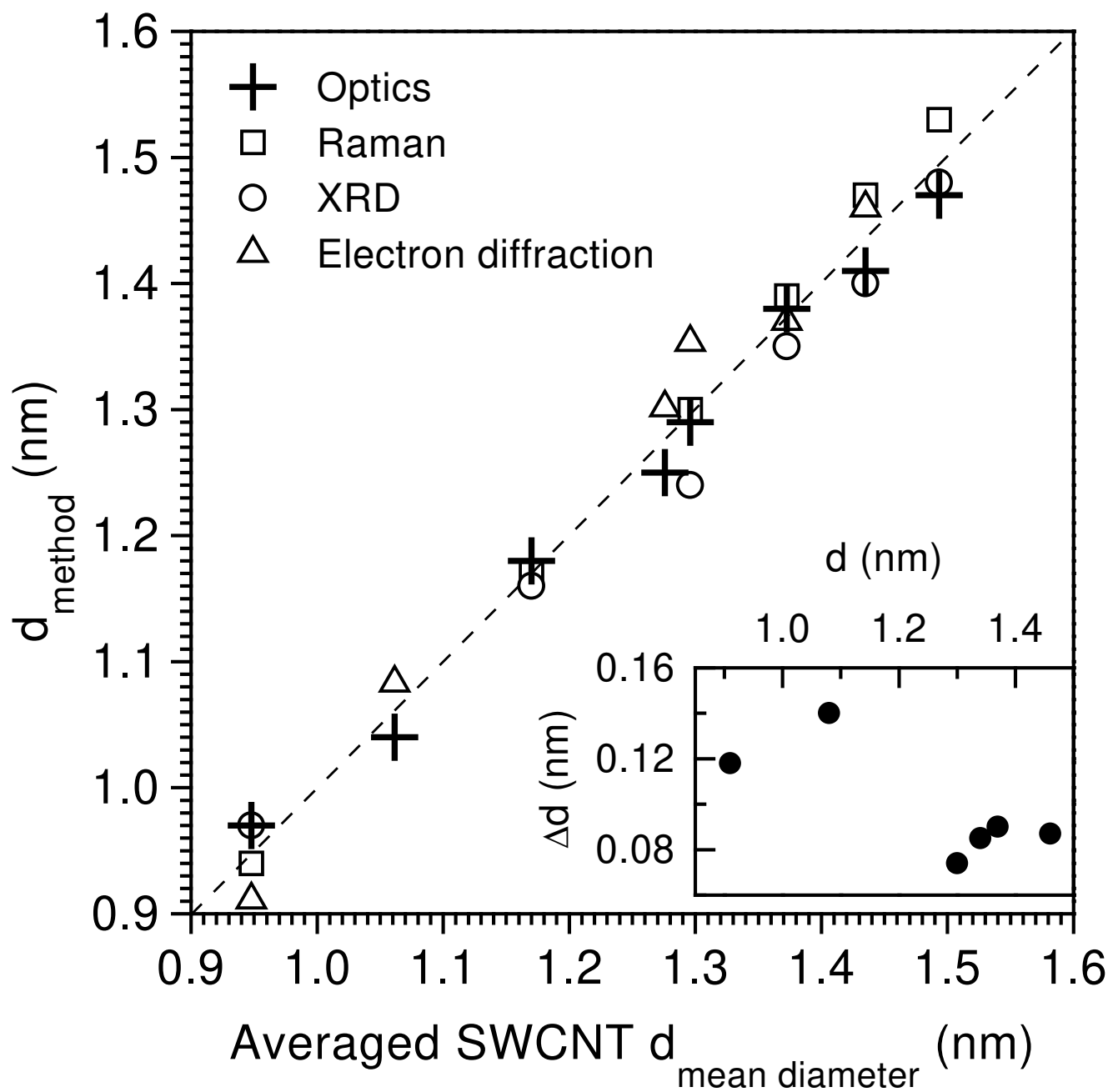


Fig. 9 Liu *et al.*

